# Ultra-fast quantification of polycrystalline texture via single shot Synchrotron X-ray/Neutron Diffraction: Methods and Assessments

Zifan Wang[1], Jingwei Chen[1], Oxana V. Magdysyuk[2], Fatih Uzun[1], Alexander M. Korsunsky[1,*]

[1]MBLEM, Department of Engineering Science, University of Oxford, Oxford OX1 3PJ
[2]Diamond Light Source, Harwell Campus, Oxfordshire, OX11 0DE, UK

Corresponding author: *

**Abstract**

Tracking texture evolution during *in situ* loading is critical to understand and simulate the dynamic behaviour of microstructure in polycrystalline materials, yet conventional texture quantification methods are sometimes restricted due to various factors, such as acquisition time, sample environment and complex setup. To address this, a novel approach to extract texture information from single shot Time-Of-Flight neutron diffraction pattern has been developed. Another texture analysis approach based on single shot synchrotron X-ray diffraction has also been demonstrated. The effectiveness of two methods is assessed for polycrystalline Nickel-based superalloy polycrystalline samples possessing different textures. Both methods feature a moderate acquisition time of ~10mins and 30 seconds respectively, as well as a simplified setup which allows adding complex sample environments and the use of additional equipment. Comparison with the referential EBSD texture suggests that both approaches achieve a satisfactory match, though some details of the complex contour profiles in inverse pole figures may be missing. Besides that, a novel metric has been proposed to quantify the matching quality of pole figures. By employing the EPSC modelling approach, it is shown that the texture deviation due to the technique chosen for its evaluation exerts a subtle influence on th macro- and mesoscale simulation results, highlighting the significance of this approach for underpinning robust computational modelling.

## 1. Introduction and objectives

Preferred crystal orientation, also known as texture, are often present in polycrystalline metallic components as a consequence of their thermomechanical history [1,2,3]. Undoubtedly, the presence of texture exerts a very strong influence on the thermomechanical and functional properties of alloys of all kinds [4], and is therefore considered as a crucial material input in dynamic modelling approaches,

such as Finite Element model [5], Crystal Plasticity Finite Element model (CPFE) [6], Visco-Plastic Self-Consistent model (VPSC) [7], Elasto-Plastic Self-Consistent model (EPSC) [8], Elasto-Visco-Plastic Self-Consistent model (EVPSC) [23].

Acquiring texture in a bulk polycrystal is usually time-consuming and requires specific instrumental setup. Conventional methods mainly include large area EBSD, synchrotron X-ray/neutron polycrystalline diffraction, and laboratory XRD diffractometry. Each of these methods has one or several drawbacks. Large area EBSD is time consuming. Prevailing EBSD systems can reach the acquisition speed of 10 frames per second (e.g. Oxford Instrument Nordlys 2013), therefore an EBSD map of adequate size for texture quantification (~$10^5$ frames) takes ~2.8 hours. In addition, EBSD technique needs strict surface preparation, and the sample surface must be kept pristine throughout measurement, thus restricting the use of sample environment such as pressure, corrosion, vibration, etc. What is more, EBSD is not applicable to materials that contain large amount of amorphous phase or nano-sized grains [9], so that only well-crystalized materials (e.g., after annealing treatment) can be used. Last, but not least, EBSD is a surface probing technique, therefore for large/bulky samples, more than one map would be necessary to confirm the texture quantification result. Complete texture determination using synchrotron X-ray/neutron polycrystalline diffraction can be achieved either by applying sample rotation [10], or by enhancing the pole figure coverage area of the detector array, like HIPPO at LANSCE [11] and GEM at ISIS [12]. The terminology "powder diffraction" is also often used to refer to the scientific technique of collecting X-ray or neutron wide angle scattering data from polycrystalline samples, so that the two terms "polycrystalline diffraction" and "powder diffraction" can be used interchangeably. Sample rotation requires a range close to 180°, within which no obstacles should be blocking the path of the X-ray/neutron beam. At facilities dedicated to texture analysis like HIPPO and GEM, detector array is arranged in such a way that covers the whole spherical space around the sample. Apparently, these two methods restrict the use of additional equipment, e.g. *in situ* loading machine, because any equipment that contacts or surrounds the sample is likely to block the diffracted beam from sample to the detector. The same principle applies to laboratory diffractometer (XRD). Therefore, in conventional SXRD/ND/XRD texture measurement setups, only initial and post-mortem texture quantification is readily feasible [11,12].

To resolve the dilemma described above, techniques have been developed to extract texture from single exposure synchrotron X-ray diffraction pattern [13,14,15,16,17,18]. In this setup, the relative position between the incident X-ray beam and the sample is fixed. The diffracted beam transmits through the sample thickness and finally reached an area detector at the back, as illustrated in Fig.1(b). Since the incident beam and the diffracted beam is small (~200μm cross-section lengths) and their travelling paths are fixed, this experimental setup gives plenty of space for additional equipment such

as *in situ* loading machine. Besides that, the 2D Debye-Scherrer ring diffraction pattern contains other valuable information such as microstrain, phase fraction, lattice strain and so on [4]. Most importantly, the acquisition for a single Debye-Scherrer ring diffraction pattern is vastly rapid owing to the high energy / flux of X-ray beam at Synchrotron facilities. For instance, the typical acquisition time for a 2mm thick Nickel-superalloy, which is considered as a high attenuation material, is merely 30 seconds at I12 JEEP beamline at DLS [13] or at ID15A beamline at ESRF [19]. The analysis routine for texture analysis based on a single Debye-Scherrer ring diffraction pattern has been partially integrated in analysis software such as MAUD [15] and GSAS-II [20].

Nevertheless, to the best of author's knowledge, the accuracy of texture being refined from such technique has rarely been verified through one of those conventional yet more reliable texture measurement methods, considering the fact that error occurs more or less due to the incomplete pole figure coverage of a single exposure synchrotron X-ray diffraction pattern [21]. Namely, there are potentially differences in Orientation Distribution Function (ODF) obtained by these texture analysis methods. Furthermore, though critical, the discrepancy in computational modelling results caused by such texture deviation (error) has never been examined. Besides that, this technique [13,14,15,20,22] is based on 2D synchrotron X-ray diffraction pattern, however, many neutron diffraction facilities for engineering strain measurement are only equipped with one detector, such as SALSA at ILL and POLDI at PSI, or two detectors, such as SMARTS at LANSCE and ENGIN-X at ISIS, capturing one or two 1D diffraction pattern(s) in a single acquisition period of ~10 minutes. An example of Time-Of-Flight neutron diffraction setup is shown in Fig.1(d). In these cases, the technique is no longer applicable.

Having identified the knowledge boundary and limitations of existing studies, the first objective of this work is to develop a novel technique that can extract texture information from a single shot Time-Of-Flight neutron diffraction (ND) pattern [23]. This novel texture analysis technique is applicable to any neutron diffraction facilities as mentioned above, viz SALSA, POLDI, SMARTS and ENGIN-X, and also other worldwide facilities that are not mentioned here. It enables texture quantification from a single shot diffraction pattern (single acquisition period), which takes around 10 minutes, without even the slightest alteration to the current diffraction setups at these facilities. This ensures the maximal flexibility of the use of any additional setups, such as sample environment equipment, loading rig, and so on. As the second objective, the texture analysis routine based on a single shot synchrotron X-ray diffraction pattern is demonstrated. This ultra-fast method allows texture quantification in ~30 seconds, depending on the X-ray energy and flux of the facility. Similarly, this method can be utilised at any beamlines with transmission diffraction capability, such as I12 at DLS, ID15A at ESRF, 1-ID at APS, and many more. Mostly importantly, the experimental setup is simple

to operate, as has been discussed above and illustrated in Fig.1(b). Advancing from previous relevant studies, the third objective of this work involves the assessment of accuracy of the texture refined from the two methods. Large area EBSD is employed to quantify the texture as reference, and being compared with textures refined from both the single shot Time-Of-Flight neutron diffraction pattern and the single shot synchrotron X-ray diffraction pattern. Pole figure matching errors are quantified by introducing a novel metric $E_p$, and a more intuitive evaluation has been made based on the plot of complete Orientation Distribution Function (ODF). Finally, as the fourth objective, the effect of texture deviation (error) on computational modelling results is examined via the texture sensitive EPSC model.

The significance of this present work is the development and verification of two ultra-fast analysis routines for texture quantification based on simple experimental setups at synchrotron X-ray facilities and neutron facilities respectively. The application of these ultra-fast analysis routines allows *in situ* texture quantification under complex sample environment. In the present study, a newly invented polycrystalline Ni-based superalloy that has great potentiality in aerospace applications is chosen as the sample for demonstration, while the analysis routines are universally applicable to all polycrystalline materials.

## 2. Experimental methods and preliminary analysis

### 2.1 Material

The specimen material used in this study belongs to a family of recently invented polycrystalline high-temperature Ni-based superalloy [24], referred to as Alloy 11. Pancake forging was conducted by isothermally and isostatically pressing a cylindrical ingot. Extracted from different locations in the pancake forged bulk, the two miniature bar samples (nominal size of $30 \times 2 \times 1$ mm$^3$) present contrasting textures. Two samples are named as Sample 1 and Sample 2 in the text below. Like other types of Ni-based superalloys, the major gamma (γ) phase of Alloy 11 has a face-centred cubic structure of H-M space group F m -3 m, of which the composition is provided in Table 1.

**Table 1**

Chemical composition of Alloy 11 (wt. %).

| Ni | Co | Cr | Ta | W | Al | Ti | Mo | Nb | Fe | Mn | Si | Zr | C | Bo |
|---|---|---|---|---|---|---|---|---|---|---|---|---|---|---|
| **bal** | 15.1 | 12.7 | 4.8 | 3.2 | 3.2 | 2.8 | 2.1 | 1.4 | 1 | 0.5 | 0.5 | 0.06 | 0.03 | 0.02 |

### 2.2 Single shot Synchrotron X-ray diffraction

The single shot synchrotron X-ray diffraction measurements were carried out at I12 JEEP beamline at Diamond Light Source, UK. The bar sample(s) was mounted statically with its largest area

surface perpendicular to the incident beam, as illustrated in Fig.1(b). Monochromatic beam energy was set to 93.7 keV with a spot size of 200μm×200μm. By moving along X and Y axis, large area diffraction mapping was conducted covering the central volume of the samples. Debye-Scherrer ring patterns were recorded by a large 2D area diffraction detector Pilatus 2M CdTe (1475×1679pixel, pixel size 172μm×172μm) sitting behind the sample. All 2D patterns from the mapping area were merged to a single pattern that represents the averaged texture of the whole area. Based on the setup calibration from Data Analysis WorkbeNch (DAWN) platform, the Rietveld analysis was performed using GSAS II [20] and visualised by MTEX [25]. For peak indexation in Fig.1(c), the Crystallographic Information File of the major γ phase refers to database code ICSD-102819.

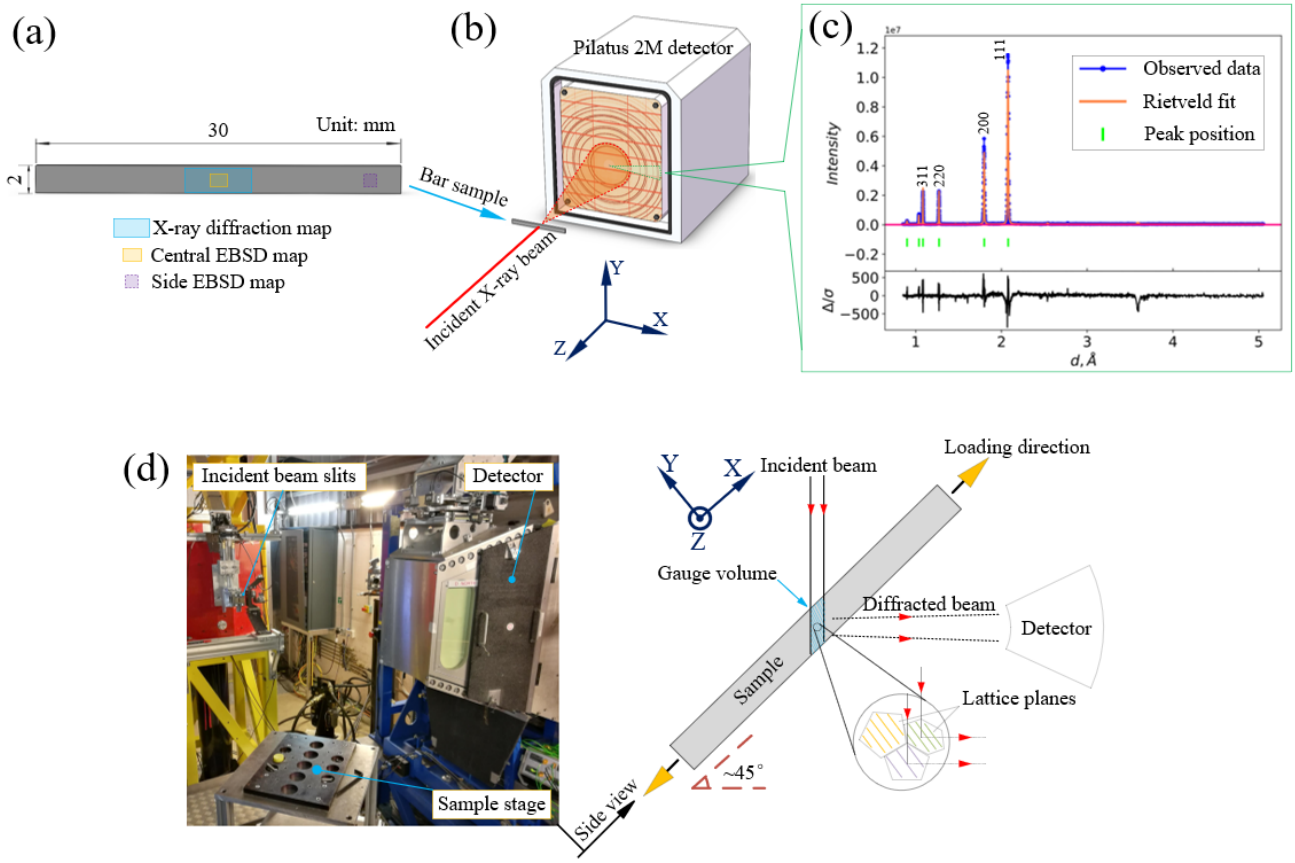


Figure 1. (a) Mapping scheme for X-ray diffraction and EBSD. (b) Overview of synchrotron X-ray diffraction setup at I12 DLS. (c) An example of integrated, indexed and refined diffraction pattern. (d) TOF neutron diffraction setup at ENGIN-X ISIS. Right hand side is a top view. The photo on the left hand side was captured from the side. Lab coordinate systems are given for both setups.

### 2.3 Single shot Time-Of-Flight neutron diffraction

The single shot Time-Of-Flight (TOF) neutron diffraction measurements were carried out at ENGIN-X hutch at ISIS, UK. As illustrated in Fig.1(d) right hand side, the bar sample was mounted horizontally at 45° relative to the incident beam. Polychromatic beam was delivered at a frequency of

50Hz with a spot size of 6mm×6mm. The beam is diffracted from lattice planes parallel to the YZ plane within the gauge volume. The 1D diffraction pattern is initially processed by the customised software OpenGenie, and imported into GSAS [20] to perform Rietveld Refinement.

### 2.4 EBSD characterization

To obtain the reference texture, electron backscatter diffraction (EBSD) observations were conducted in a Tescan LYRA3 system integrated with the superb SYMMETRY CMOS EBSD detector from Oxford Instruments. Samples were polished step by step till 0.25μm colloidal silica. Indexation of Kikuchi patterns was carried out under 20kV, 10mm working distance, and ~0.5 μm step size.

A rigorous strategy is followed to ensure the accuracy of reference texture. In the first instance, a large EBSD map (1.5mm×1mm) was acquired at the same central area as that of the X-ray diffraction mapping on each sample, as shown in Fig.1(a). In the second instance, another map (1mm×1mm) was acquired at the side region away from the central area. Then the pole figures that are constructed from the two maps are compared to ensure that the texture is consistent across the sample. Finally, the textures from two maps are combined as the reference texture of that sample. The reference texture is referred to as EBSD texture in the text below. Pole figures of the two maps and their combination are shown in Fig.5&6.

## 3. Texture analysis techniques

### 3.1 Single shot Time-Of-Flight neutron diffraction

Neutrons and X-rays interact with matter differently in such a way that neutron interact directly with nucleus of atoms while X-rays interact with the electron cloud surrounding atoms. For powder diffraction of polycrystals, the two techniques are similar, except the minor variance in diffraction intensity [26]. What is more, this difference can be compensated by detector calibration using reference crystals. Hence single shot Time-Of-Flight neutron diffraction pattern is substituted by a portion of synchrotron X-ray diffraction pattern, as shown in Fig.2(a).

#### 3.1.1 Theoretical intensity and texture effect

Assuming a polycrystalline aggregate of any texture, and by taking into account the scattering geometry, crystallographic information, and detector calibration result, the theoretical diffraction profile can be estimated by a mathematical model [27]:

$$I_T = I_B + I_D = I_B + \sum_h S \cdot K \cdot F_h^2 \cdot P(\Delta T_h), \quad (1)$$

where $I_T$ is theoretical intensity, $I_B$ is background intensity. The last term $I_D$ is diffraction intensity, which is a sum of contributions from each reflection $h$. Every contribution is multiplication of structure factor $F_h^2$, scale factor $S$, correction factor $K$, and peak profile function $P(\Delta T_h)$. The value of correction

factor $K$ is partially determined by another factor $A(h, y)$ that describes the variation of diffraction intensity due to texture effect:

$$A(\varphi, \beta, \psi, \gamma) = 1 + T, \quad (2)$$

where T is expressed by the generalized spherical-harmonics term:

$$T = \sum_{l=2}^{L} 4\pi/(2l+1) \sum_{m=-l}^{l} \sum_{n=-l}^{l} C_l^{mn} k_l^m(\varphi, \beta) k_l^n(\psi, \gamma), \quad (3)$$

where $C_l^{mn}$ are harmonic coefficients, which can be determined by Rietveld refinement, and the two harmonic terms, $k_l^m$ and $k_l^n$ depend on the crystal and sample symmetries respectively [28], therefore the two inner summations depend on the unique, nonzero harmonic terms. The selection of the two harmonics terms is profoundly affected by the assumption of sample texture symmetry. What is more, various orders of the spherical harmonics equation can be chosen in order to adapt the diverse degree of complexity of the diffraction pattern. For pattern with fewer diffraction peaks, the number of order can be selected from four to eight, while for pattern with more diffraction peaks, the number of order can be selected up to fourteen. The higher the order, the larger number of harmonic coefficients in Eq.3. This offers great flexibility and robustness in quantifying the texture effect from the diffraction pattern. With this advancement, it becomes possible to extract texture information from merely a single diffraction pattern. Compared with conventional methods that relies on the input from tens / hundreds of diffraction patterns, relying on a single pattern ensures the ultra-fast feature of this texture quantification technique.

Apparently, in the case of an ideal polycrystalline material of random texture, $T = 0$. Take {111} reflection for instance as shown in Fig.2(b), $I_D$ represents its intensity without the correction of texture effect. At this initial stage of refinement, there is a gap between observed data and Rietveld fit. Upon refining, the texture effect is corrected so that the intensity matches with observed data as shown in Fig.2(c). The intensity of {111} has been corrected from $I_D$ to $I_D'$. Besides that, intensities of all other reflections in Fig.2(c), e.g. {200} and {220}, have also been corrected by taking into account the texture effect. These intensity corrections are recorded by the harmonics coefficients $C_l^{mn}$ in Eq.(3), which contain quantitative orientation distribution of grain families of all reflections that are available in the diffraction pattern. Namely, the populations of grains that contributes to certain reflections are quantified. The proportion of the actual population to that of the ideal random texture state is termed Multiples of Random Distribution (MRD).

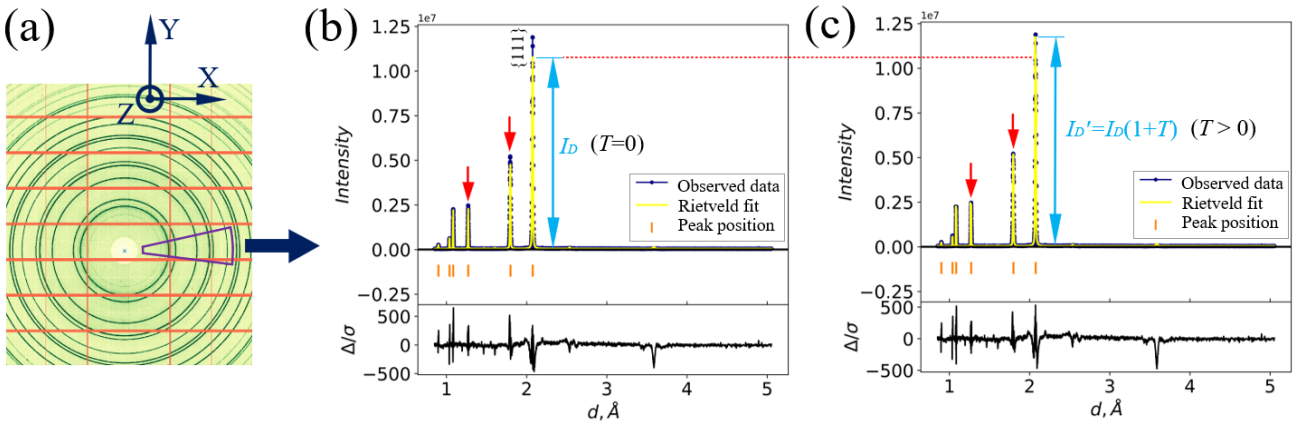


Figure 2. (a) Diffraction pattern from Sample 1 integrated around 15° azimuth in X direction. (b) Rietveld refinement without considering texture effect. (c) Correction of diffraction intensity via variation of grain population of all reflections in X direction.

3.1.2 Justification of cylindrical symmetry

During the texture analysis using Eq.(3), the population of grains whose {*hkl*} reflection normal vectors are parallel to the diffraction scattering vector is quantified. However, the orientation information of how those grains rotating around that {*hkl*} reflection normal remains missing. Therefore, cylindrical symmetry must be chosen, assuming that those grains distribute homogeneously around that particular {*hkl*} normal vector.

Take the {111} reflection as an example, as depicted in Fig.3(a). Suppose that the population of grains whose {111} reflection normal vectors are parallel to the X direction is quantified via the theory introduced in Section 3.1.1. Since the quantity of <111> vector is known and the crystal structure is fixed, the quantity of <110>, <100>, <311> vectors in certain directions (pointed by the arrows in Fig.3(a))can be deduced, so as the corresponding lattice planes, namely {220}, {200}, {311}, etc. Nevertheless, as indicated by the circular yellow arrow, it cannot be determined how these crystals population distribute around the <111> direction, thus homogeneous distribution is presumed.

Based on the cylindrical symmetry and 8-order spherical harmonics, a series of inter-related pole figures can be constructed from the refined harmonics coefficients, as shown in Fig.3(b). The inter-relation can be explained in such a way that for each pole figure, only the intensity at the centre of the circle, i.e. projection of MRD parallel to the X direction, is directly refined from the texture correction of peak intensity from a diffraction pattern (Fig.2), whilst the intensity of the remaining area is deduced from central intensity of other pole figures. For instance, in Fig.3(b), the {111} pole figure centre has a low intensity of 0.8 MRD. According to the geometry of crystallographic reflection planes depicted in Fig.3(a), this causes the low intensity in {200}, {220}, {311} reflections in certain directions. As pointed out by the black arrows, this is reflected by the low intensity annular regions in the latter three

pole figures {200}, {220} and {311}. The corresponding annular regions are marked by the dashed lines using the same colours as the colour of {*hkl*}, viz the top line indicates the diameter of the low intensity annular regions of {200} pole figure, the bottom line indicates the diameter of the low intensity annular regions of {311} pole figure. The diameters of these annular regions match well with relative geometry of *hkl* reflections in Fig.3(a). The blue colour of these marked annular regions indicates their low MRD as a consequence of the low intensity at the centre of {111} pole figure.

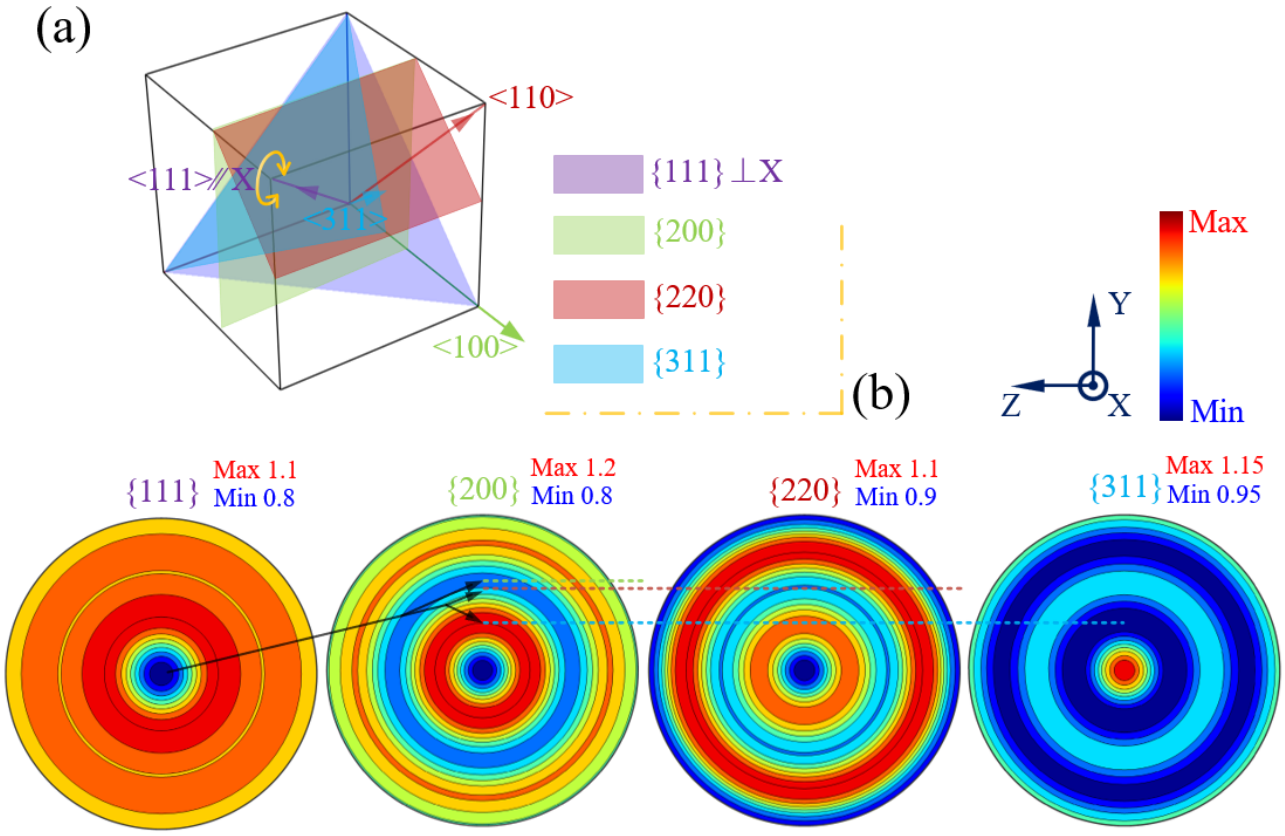


Figure 3. (a) Geometry of crystallographic reflections in FCC crystal, with {111} plane normal parallel to the X axis. (b) Constructed pole figures from single shot diffraction pattern of sample 2, in unit of MRD. Colour of dashed lines corresponds to the colour of {*hkl*} indices.

3.1.3 ODF construction

The ODF can be reliably estimated from pole figures through a novel analysis routine introduced in [29]. Mathematically, the pole density function P with respect to the ODF can be expressed by a fundamental texture analysis equation [30]:

$$P(h,r) = \frac{1}{2}[\mathcal{R}f(h,r) + \mathcal{R}f(-h,r)], \quad (4)$$

where $f$ is the ODF, $\mathcal{R}$ is the integral operator recognized as the geodesic Radon transform.

Based on Eq.4, the statistical model can be written as:

$$I_{ij} \simeq Pois\left[I_{ij}^{b} + [v_{true}]_i \mathcal{R} f_{true}(H_i, r_{ij})\right], \quad (5)$$

where $I_{ij}$ is the statistical counts, $I_{ij}^{b}$ is the background counts. $Pois$ means the parameterized Poisson process.

The ODF construction is equivalent to the classical parameter estimation. Given a random sample $I_{ij}$, $i$=1,…, $N$, $j$=1,…, $N_i$ of counts, the modified least squares estimator can be written as:

$$f_{MLS} = \operatorname{argmin} \sum_{i=1}^{N} \sum_{j=1}^{N_i} \frac{|\alpha_i \mathcal{R} f(h_i, r_{ij}) - I_{ij}|^2}{I_{ij}}, \quad (6)$$

which includes a series of unknown normalization coefficients as variables. To numerically solve the minimization problem of Eq.6 requires discretization of ODF, which is approximated by Fourier expansion. The Fourier expansion can be identified as a composition of a spherical and an adjoint spherical Fourier transform. Finally, a modified steepest descent algorithm is applied to solve the minimization problem. The algorithm has been implemented in the texture analysis software MTEX. The pole figures constructed in Section 3.1.2 can be imported into the software, from which the ODF is estimated and inverse pole figures constructed.

### 3.2 Single shot synchrotron X-ray diffraction

For a single synchrotron X-ray diffraction pattern, the texture analysis routine has been elucidated in previous studies [20]. In the present work, 24 patterns are integrated around the diffraction rings with a step size of 15°, as illustrated in Fig.4(a). Pole figures and inverse pole figures are constructed based on the refined harmonics coefficients in GSAS II, as shown in Fig.4(b). No sample symmetry and 8-order spherical harmonics are assumed. The figures are then imported into the MTEX software for plotting and comparison in Section 4.2.

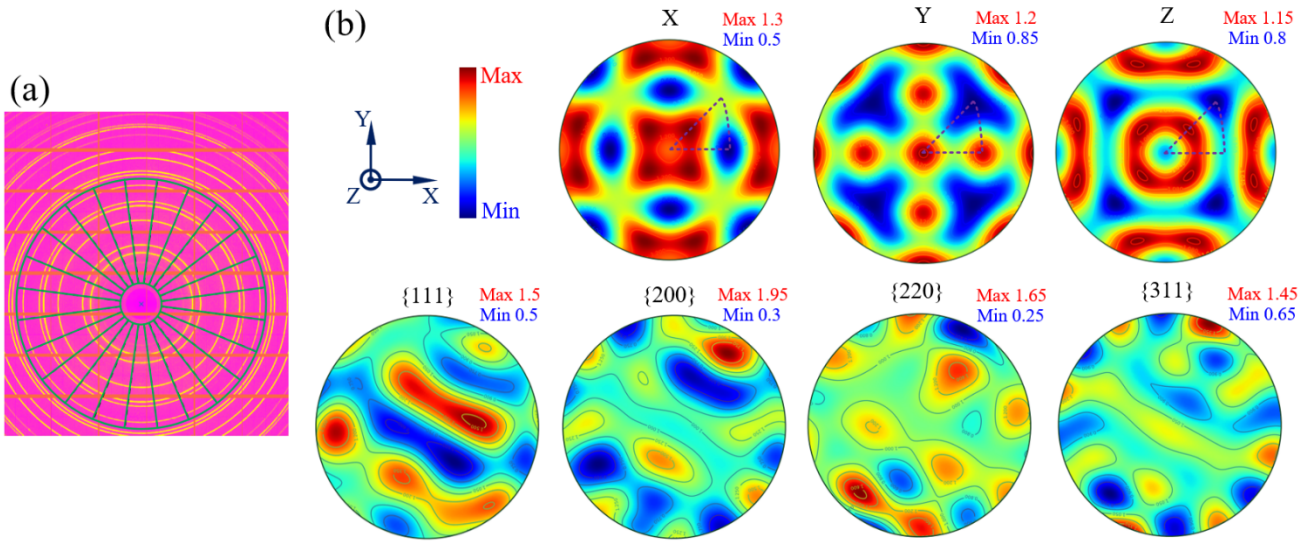


Figure 4. Texture analysis example of sample 1. (a) 24 segmentations of synchrotron X-ray 2D

diffraction pattern. (b) Inverse pole figures and pole figures constructed from harmonics coefficients in GSAS II, in unit of MRD. Inverse pole figures are given in complete projection space, but the fundamental region for cubic structure is highlighted in dashed triangle.

## 4. Results and discussion

### 4.1 EBSD maps and EBSD texture

The EBSD maps and texture information of Sample 1 and Sample 2 are shown in Fig.5 and Fig.6 respectively. Each map consists of a statistical counting of approximately half million grain orientations, from which pole figures are constructed. The four reflections of pole figures, namely {111}, {200}, {220} and {331} are selected according to the strongest diffraction peaks in Fig.1(c).

The grain orientation statistics of Sample 1 exhibits such distribution that does not belong to any commonly observed texture types. The highest / lowest intensity area dot around the whole hemisphere of the four pole figures. Nevertheless, the pole figures of central and side EBSD mapping area match well with each other in terms of maximum/minimum MRD value, contour profile and intensity distribution. This confirms the uniformness of texture across the length scale in Sample 1. Therefore, the EBSD texture, which represents the standard reference texture of the entire sample, can be established by synthesising texture from the two maps, as shown in Fig.5(c). Additionally, inverse pole figure in three principal directions (X, Y and Z) are given for comparison in Section 4.2.

Comparatively, the grain orientation statistics of Sample 2 demonstrate pretty much the same features as were observed in Sample 1, except the smaller grain size and less texture complexity. Fig.6(c) shows the EBSD texture of Sample 2.

The textures of Sample 1 and Sample 2 are relatively weak since the maximum MRD is less than 2, yet the preferred grain orientations are totally different. This makes them challenging practices as well as tenable verifications for the texture analysis techniques in this study.

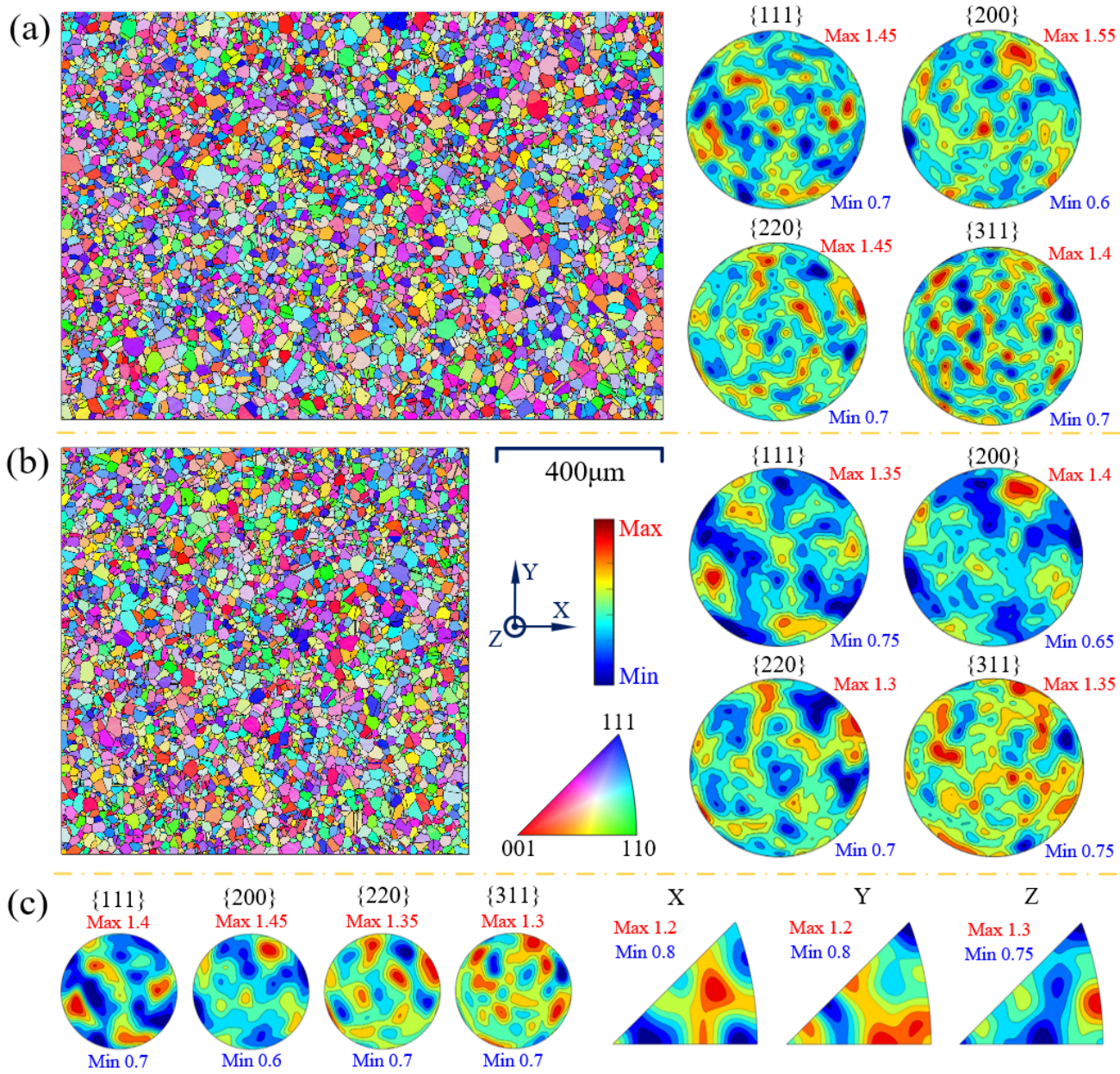


Figure 5. EBSD measurements of Sample 1. EBSD map scale bar, coordinate system for EBSD map and pole figures, colour key for Multiples of the Random Distribution (MRD), and colour key for EBSD maps in Z direction are presented together in the middle. (a) Central area map and pole figure texture statistics. (b) Side area map and pole figure texture statistics. (c) EBSD texture, a combination of texture statistics of both maps.

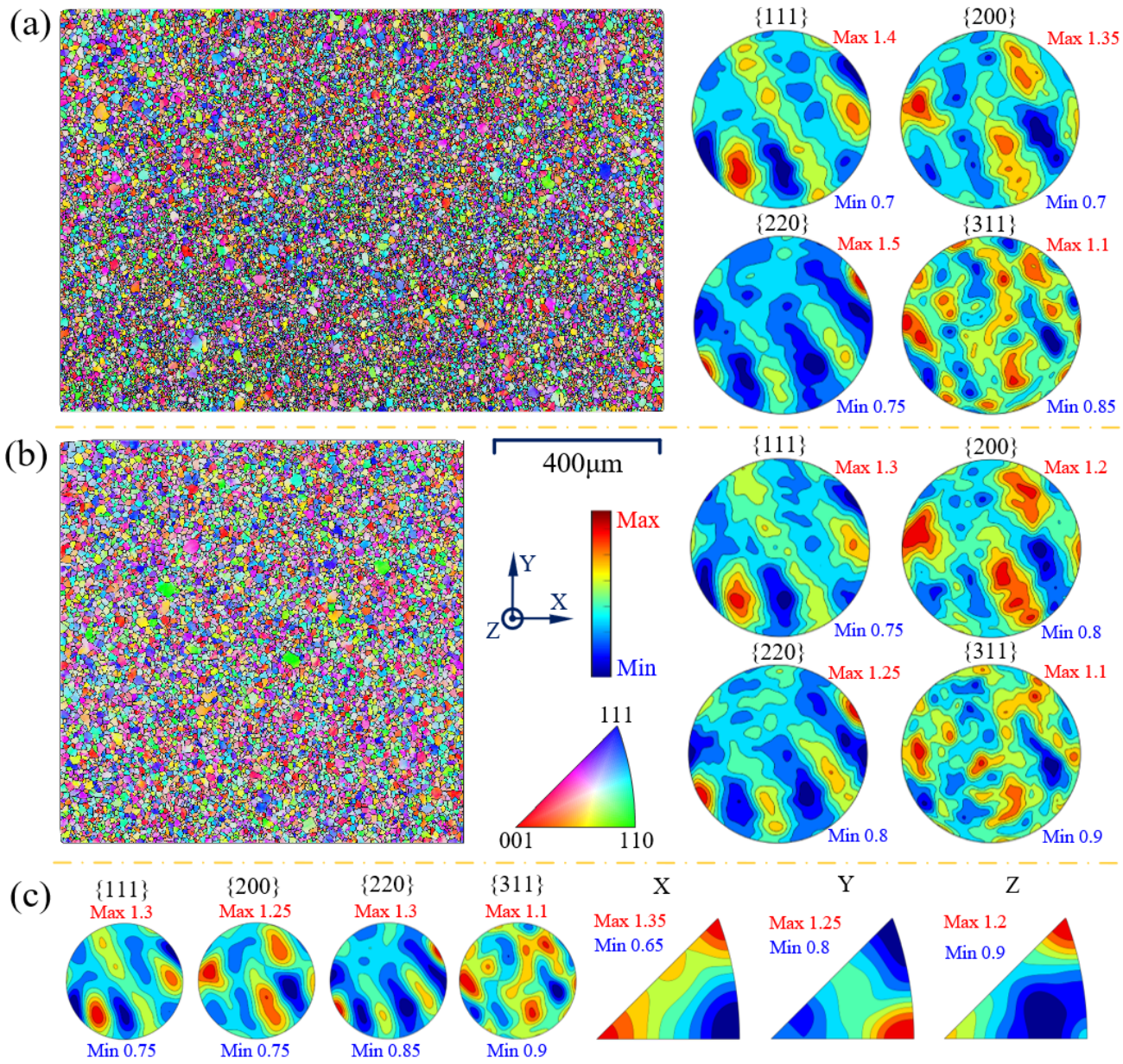


Figure 6. EBSD measurements of Sample 2. For detailed caption please refer to that of Fig.5.

### 4.2 Comparison of texture results

Based upon the texture analysis techniques being introduced in Section 3, texture information can be derived from diffraction patterns of both experimental setups, namely single shot Time-Of-Flight neutron diffraction and single shot synchrotron X-ray diffraction. For the purpose of accuracy assessment, results are plotted in contrast with the referential EBSD texture, as shown in Fig.7 and Fig.8 for Sample 1 and 2 respectively.

The texture results from single shot Time-Of-Flight neutron diffraction are shown in Fig.7(b) and Fig.8(b). As has been discussed in Section 3.1, a single diffraction pattern contains texture information of a specific direction, thus only inverse pole figure of that direction may be accurately constructed.

Hence for each sample, two segmentations in the X and Y directions are made to produce two inverse pole figures. Compared with EBSD texture plots, single shot neutron diffraction well captures the overall texture in terms of intensity distribution and max/min intensity, for instance, <111>, <001> and <110> in both X and Y in Fig.7(b), similar in Fig.8(b). However, the detailed contours are blurred, such as Fig.7(b) Y direction, that the plot indicates the intense region in the middle of the triangular area, whilst the actual distribution consists of three peak regions (Fig.7(a) Y direction). The reason why the texture at <111>, <001> and <110> directions correspond well with the EBSD observation than other directions is obvious: their diffraction peaks are directly observable from the pattern (e.g. Fig.1(c)) whose intensities are corrected by texture effect.

The texture results from single shot synchrotron X-ray diffraction are shown in Fig.7(c) and Fig.8(c). Incomplete pole figures can be constructed from the input of 24 diffraction patterns around the azimuthal direction. Regarding Sample 1, pole figure contours exhibit decent matching between Fig.7(a) and Fig.7(c), particularly the most/least intense regions, though some deviations can be observed. The matching of pole figures in Sample 2 between Fig.8(a) and Fig.8(c) is better, especially the {111} and {220} plane groups. To quantify the matching quality, the difference pole figures are provided in Fig.7(d) and Fig.8(d), together with the novel metric $E_p$ that evaluates the error between two pole figures. Metric $E_p$ is defined as: $E_P = \frac{1}{n}\sum_1^n \frac{|M_i - N_i|}{M_i}$, where $M_i$ is the MRD value at a point in the EBSD pole figure, $N_i$ is that in the diffraction pole figure, $n$ is the number of discretised points in the pole figure domain. The calculated $E_p$ values suggest that the errors are generally below 10% (10%=0.1), the average is around 5%. For a better visual evaluation, a quantitative comparison of complete ODF is made by plotting the ODF difference between EBSD reference and our analysis technique, as shown in Fig.7(e) and Fig.8(e). For FCC crystal structure, the standard Euler angle range is a 90°×90°×360° space, thus 9 sections are plotted at a step size of every 10°. It can be seen that the majority of ODF space shows a difference of 0-0.1 MRD for both Sample 1 and Sample 2. The accuracy of texture analysis of Sample 2 is slightly better because of less regions with peak values. Therefore, from both the parametric and visual evaluation, the result of our texture analysis technique exhibits decent agreement with EBSD. The comparison of complete ODF between EBSD and synchrotron X-ray diffraction is presented in Fig.9 and Fig.10 for Sample 1 and Sample 2, respectively.

It is note-worthy that the inverse pole figures of Sample 2 show excellent matching with EBSD in X and Y direction, whilst that of Sample 1 is more deviated but acceptable. Compared with inverse pole figures from neutron diffraction, those from synchrotron X-ray diffraction contain more details, though still not enough to capture the profile. Due to the combination of patterns from 24 azimuthal directions, single shot synchrotron X-ray diffraction provide texture information of satisfactory

precision.

Nevertheless, it should be pointed out that the Z direction inverse pole figures from single shot synchrotron X-ray diffraction exhibit poor matching with EBSD result in both Sample 1 & 2. Reason is fairly straightforward, that the Z direction is parallel to the incident beam where lacks the diffraction information, leading to the faulty texture prediction.

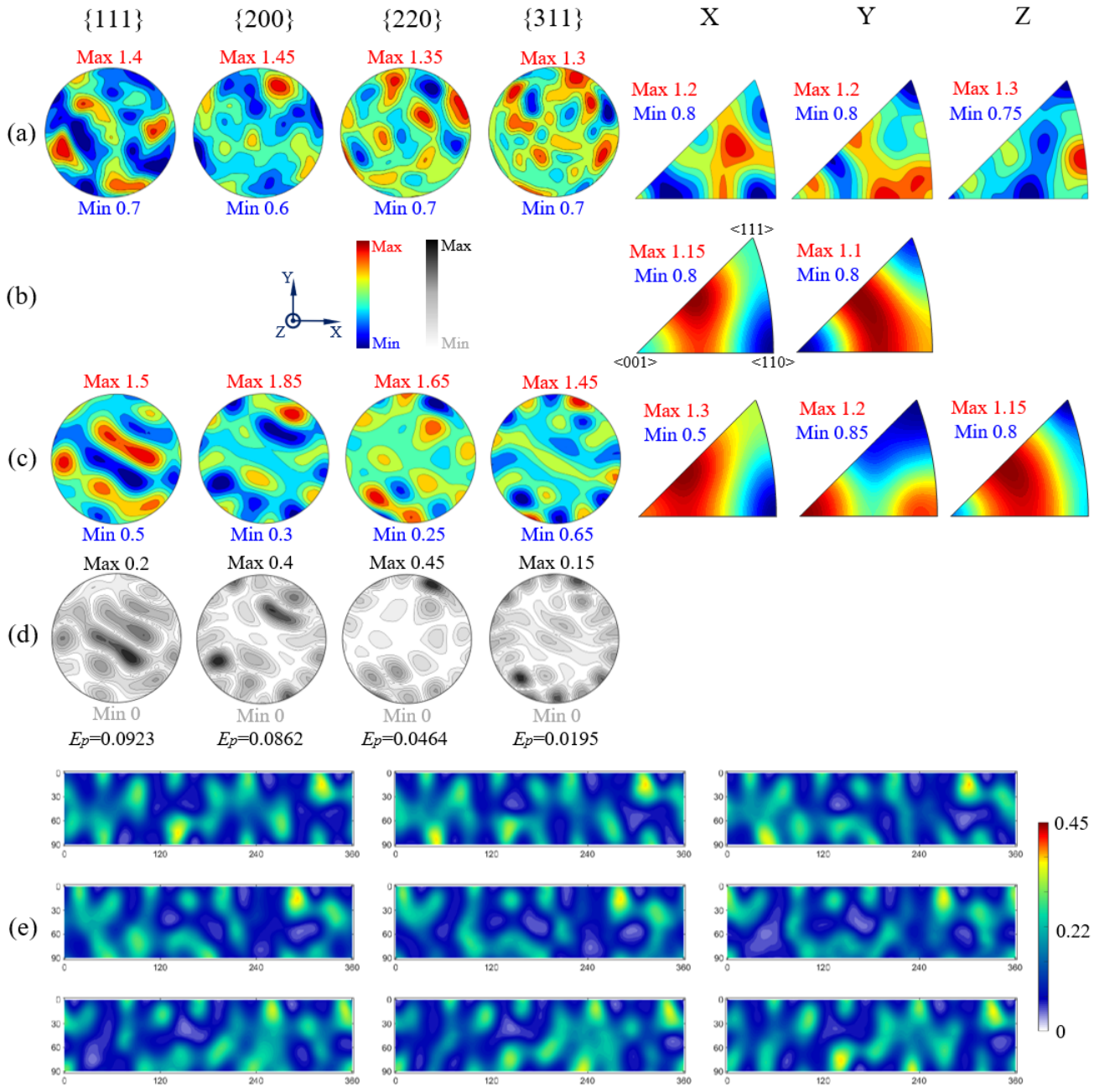


Figure 7. Comparison of texture results of Sample 1. Coordinate system and intensity colour key are near the picture centre, in units of MRD. Four *hkl* indices for pole figures and three directions for inverse pole figures are on the top line. (a) Referential EBSD texture. (b) Single shot Time-Of-Flight neutron diffraction pattern. (c) Single shot synchrotron X-ray diffraction. (d) Difference pole figures

between EBSD and single shot synchrotron X-ray diffraction, with corresponding $E_p$ values that indicate the matching quality. (e) Difference of complete ODF space between EBSD and single shot synchrotron X-ray diffraction, in unit of MRD. Top left is 0° section, and bottom left is 90° section.

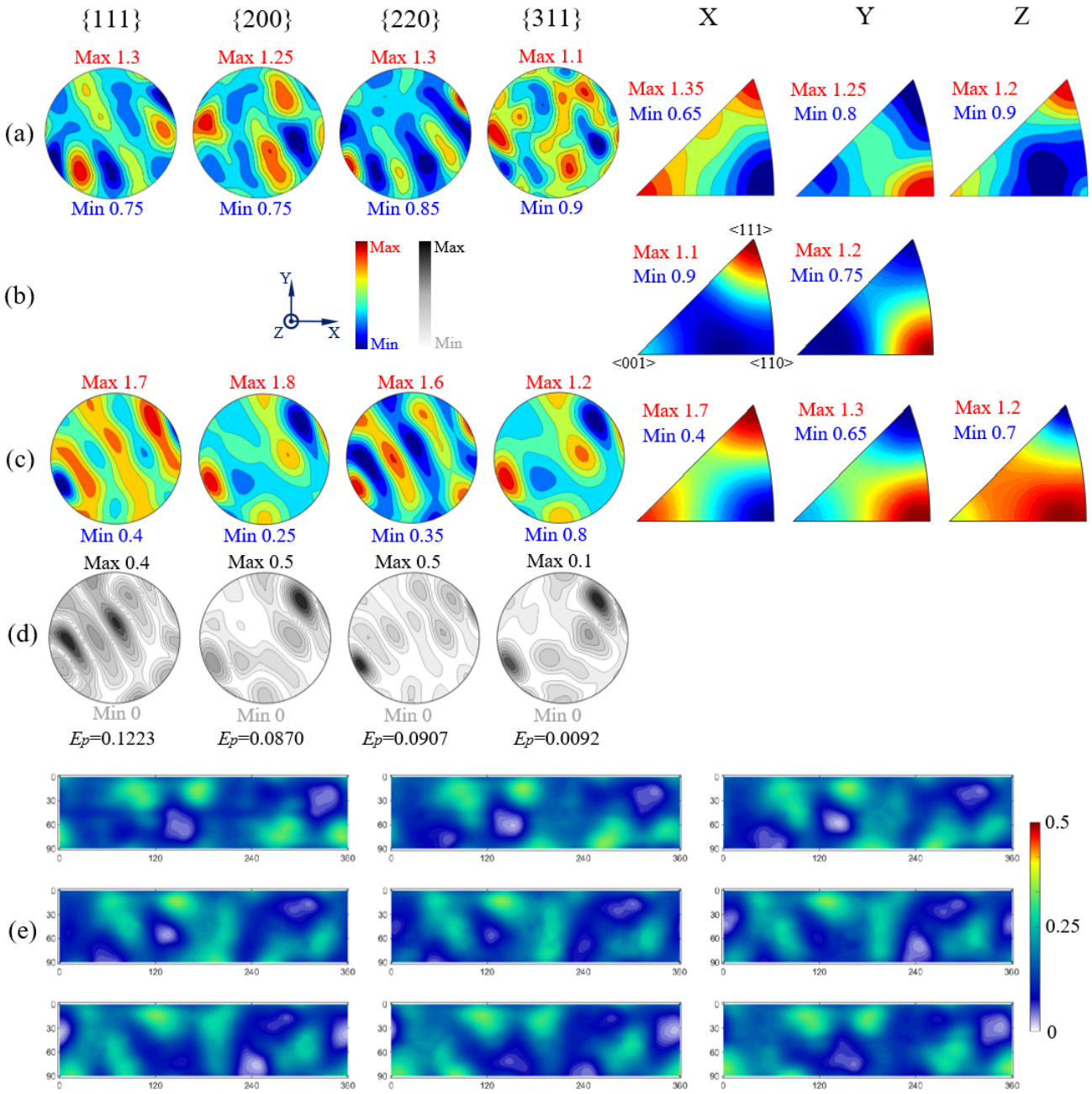


Figure 8. Comparison of texture results of Sample 2. For detailed caption please refer to that of Fig.7.

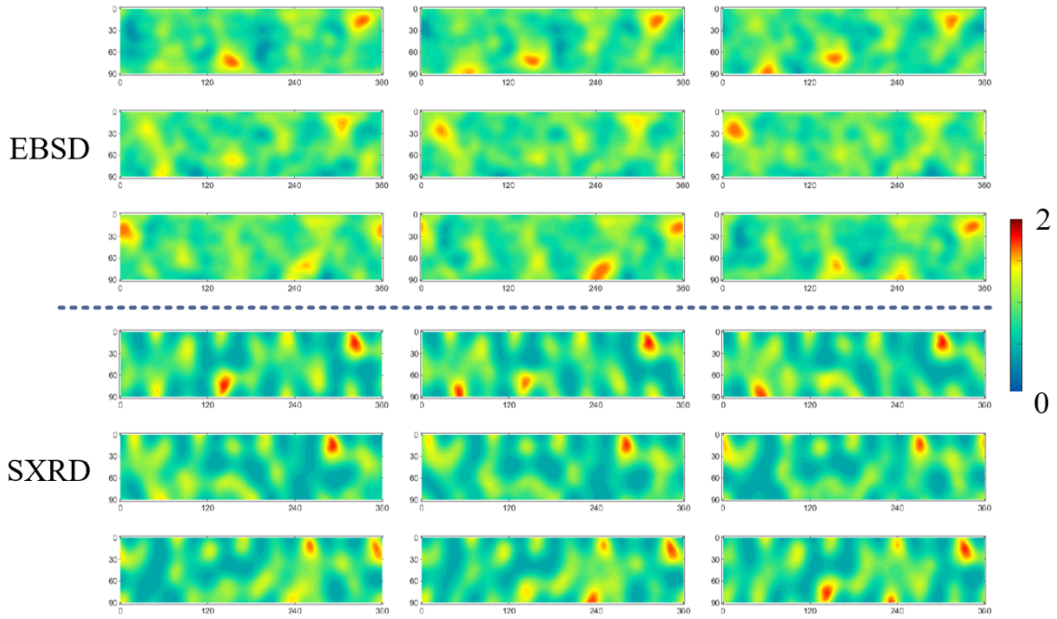


Figure 9. Comparison of complete ODF obtained from EBSD and SXRD of Sample 1.

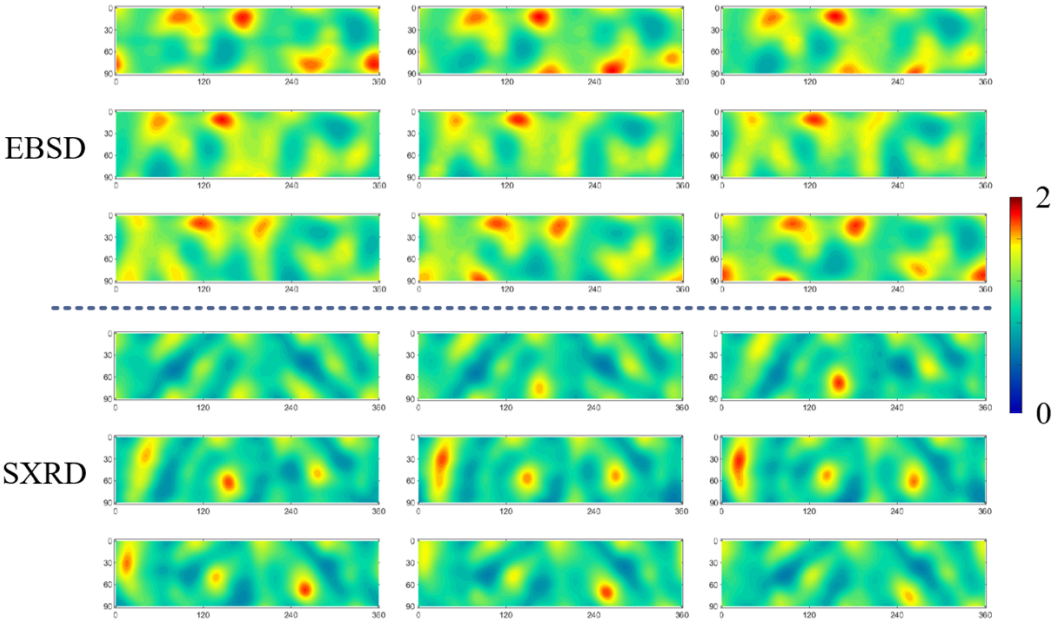


Figure 10. Comparison of complete ODF obtained from EBSD and SXRD of Sample 2.

### 4.3 Effect of texture deviation on modelling approach

In Section 4.2, visual comparison has been made between the referential EBSD observation and diffraction results. For texture analysis techniques, deviations occur more or less, whose randomness is rather difficult to quantify. In practice, texture refined from diffraction patterns is used to predict material's thermomechanical properties, via either empirical or advanced modelling approaches. Therefore, what really concerns is the effect of such random deviations on modelling result, as is the

topic of this section.

4.3.1 EPSC modelling approach

The Elasto-Plastic Self-Consistent (EPSC) modelling approach treats grains as ellipsoidal inclusion embedded in a homogeneous medium. Based on the Eshelby theory, the model implements Voce-type hardening law to describe the activation and hardening of slip system *s*:

$$\hat{\tau}^s = \tau_0^s + (\tau_1^s + \theta_1^s \Gamma)\left(1 - e^{-\left(\frac{\theta_0^s \Gamma}{\tau_1^s}\right)}\right), \quad (7)$$

where Γ is the accumulated shear in the grain, $\tau_0$, $\tau_1$, $\theta_0$, $\theta_1$ are hardening parameters. Detailed numerical implementation of the model refers to [8]. The tenability and universality of the EPSC model and its modified version has been validated by numerous studies in the past 30 years, including but not limited to [4,7,8,31,32]. In this study, the Version 4 is used, which was developed in recent years.

The model is calibrated through fitting macroscopic stress-strain behaviour with tensile loading experiment for a Ni-superalloy sample of random grain orientation distribution, as shown in Fig.11.

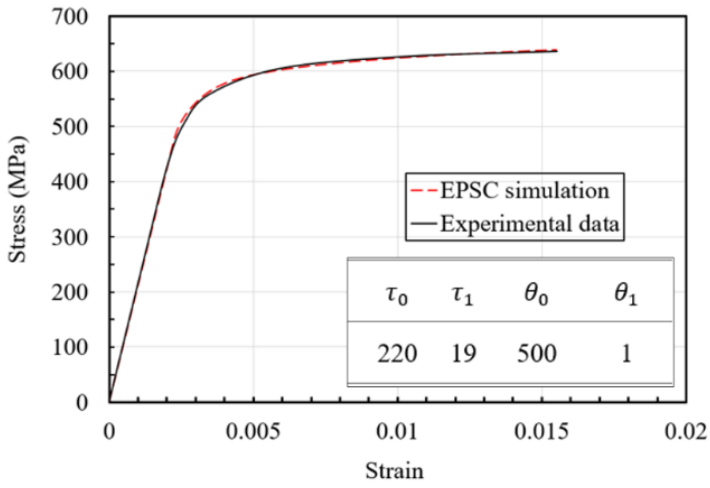


Figure 11. The EPSC model is calibrated with experimental data. Hardening parameters are tuned as shown in the table.

4.3.2 Effect of texture deviation on macroscale simulation results

The grain population file of the calibrated EPSC model is created by random sampling from the texture of EBSD and single shot synchrotron X-ray diffraction (below abbreviated as SXRD). 50000 orientations are randomly sampled from the constructed ODF using the discrete sample function integrated in MTEX. The grain ellipsoidal ratios for both samples are set to 1, viz equivalent to round shape. Texture evolution mode is enabled. Simulation was conducted in strain control mode, with a step size of 0.0001, altogether 200 steps from 0 till 0.02. Loading axis is set parallel to the X direction in Fig.1, and stress in Y and Z direction is set to 0. Strain in Y and Z and stress in X direction are

outputs from the simulation.

The macroscopic stress-strain loading simulation result is shown in Fig.12. The four curves show negligible difference in the elastic regime from 0 to 500 MPa. The yielding points are about the same level, whilst the texture exerts a huge influence on the hardening behaviour. Two curves of Sample 1 seem to exhibit a more gradual hardening than the Sample 2, clearly the four curves are separated into two distinct groups for different samples. The difference in stress-strain curve in the initial plastic regime between the two samples may be attributed to the enabled texture evolution mode in the simulation, while such discrepancy shows a tendency of convergence beyond the strain level of ~1.2%. The final textures of both samples are displayed in Fig.13. It can be clearly observed that divergent strong textures of which local MRD larger than 4 were developed from the weak texture. This observation agrees well with previous study of the same model [32]. It is obvious that this intense reorientation activity results in the discrepancy in the plastic regime.

A zoom in view of plastic regime is displayed in the blue insert map in Fig.12. The two curves of EBSD texture and SXRD texture from Sample 1 fall more apart than Sample 2, agreeing well the fact that in the visual comparison of pole figures in Section 4.2, there shows a better match between EBSD texture and SXRD in Sample 2, which leads to a nearly identical curve paths. What is more, the curves of Sample 1 remain steadily parallel with each other, not in a diverging manner.

Overall, it can be concluded that effect of texture deviation brought by the texture analysis technique is much less than that caused by the diversity of texture in different samples, even for weak textures, i.e. maxima less than 2 MRD.

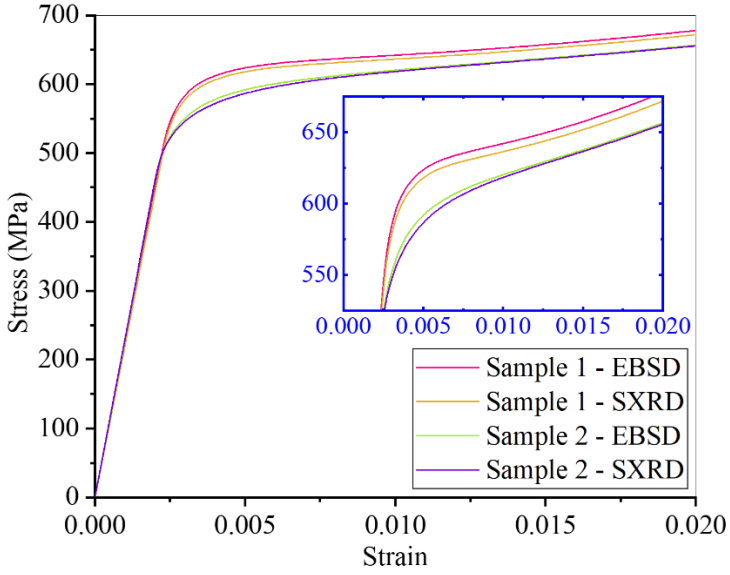


Figure 12. Macroscopic stress-strain loading simulation result from EPSC model. EBSD texture and single shot synchrotron X-ray diffraction (SXRD) texture files are used, presented by curves in different colours.

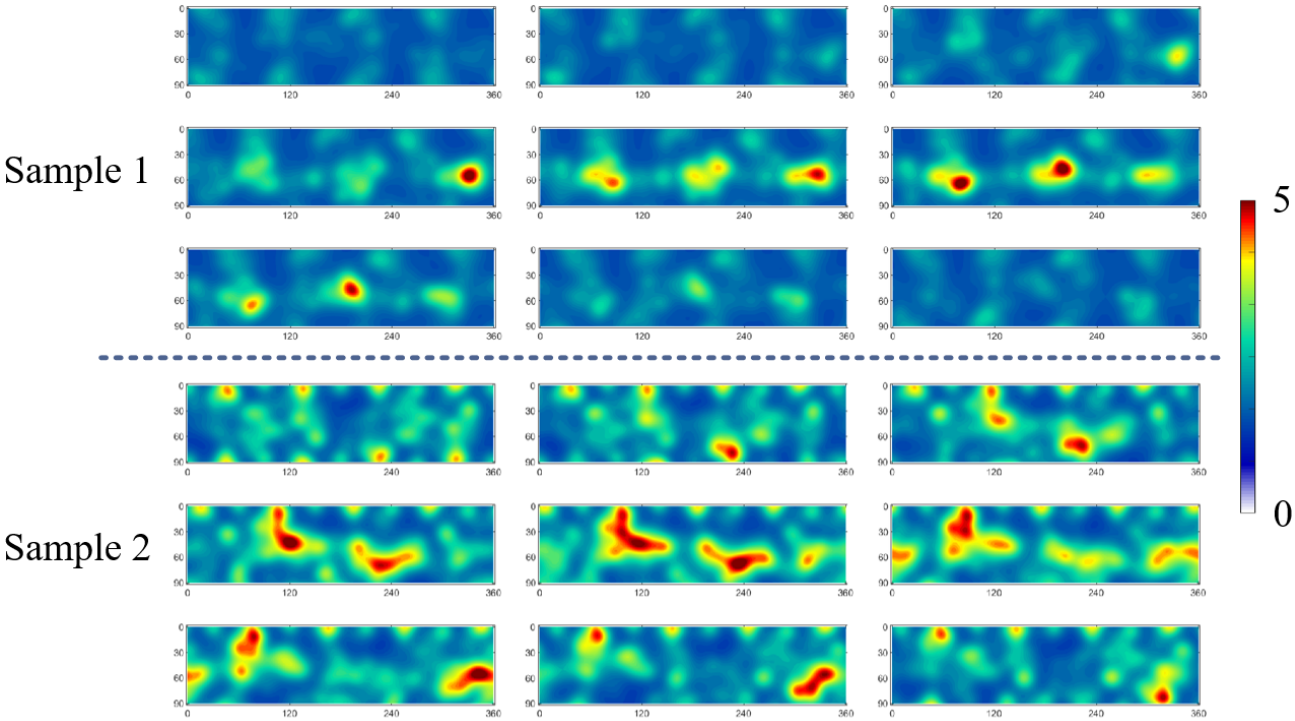


Figure 13. Final textures for Sample 1 and Sample 2 at 2% tensile elongation from the EPSC model. The complete ODF of each sample is a summation of EBSD and SXRD.

4.3.2 Effect of texture deviation on mesoscale simulation results

Considering the fact that synchrotron X-ray diffraction provides mesoscale information of polycrystalline, which means the combination of grains that contribute to certain reflections as grain groups, within the gauge volume that is illuminated by X-ray beam, it is necessary to exam the mesoscale simulation results, as shown in Fig.14.

Comparing Fig.14(a)&(b), it is obvious that intrinsic texture in Sample 1&2 brings about different lattice strain evolution paths in both directions. In Axial Direction, the lattice strain paths of EBSD texture and SXRD texture show excellent match without visible diversity. By contrast, the paths split in the plastic regime in both samples in Radial Direction, for Sample 1, the divergence is larger, which explains the observation in its macroscopic curves. Despite that, the curves of the same grain group still follow the same tendency regardless of the extent. Additionally, the quantity of grains included in this simulation has been proved to be adequate to achieve a stable result, since a 20000 grain aggregate produces exactly the same stress-strain curve.

Overall, it can be concluded that the effect of texture deviation from texture analysis technique brings about subtle mismatch in the behaviour of grain groups in Radial Direction, whilst negligible in Axial Direction.

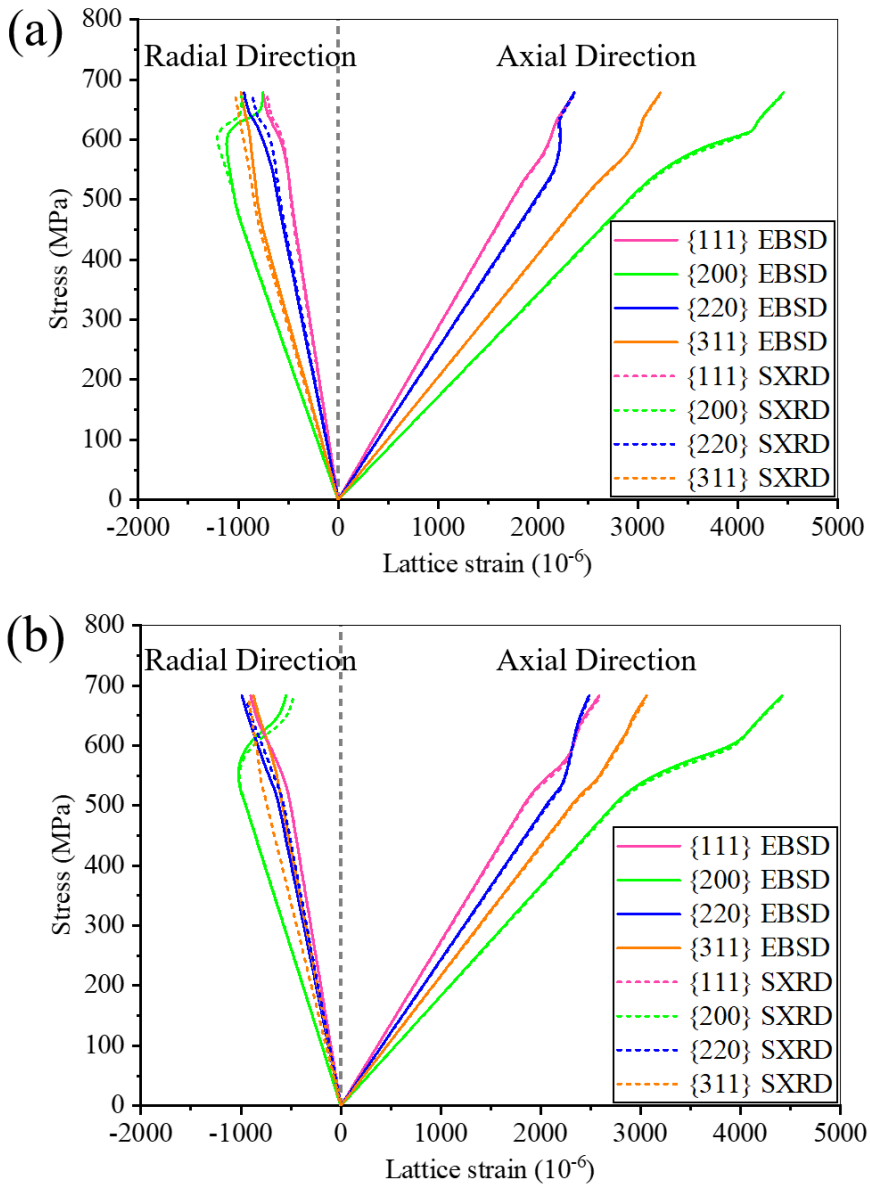


Figure 14. Lattice strain of {*hkl*} grain groups in loading direction (Axial Direction) and its vertical (Radial Direction). Results of EBSD texture are presented in solid lines whilst those of SXRD texture are in dashed lines (a) Sample 1. (b) Sample 2.

## 5. Summary and conclusions

In the present work, two ultra-fast texture analysis techniques have been developed and demonstrated. Firstly, a novel texture analysis method based on single shot Time-Of-Flight neutron diffraction (ND) pattern is elucidated. Secondly, texture analysis from single shot synchrotron X-ray diffraction (SXRD) pattern is conducted. Both techniques are based on experimental setups that are simple to establish. Pole figures and inverse pole figures constructed from both texture analysis methods are assessed through comparison with the referential texture quantified by large-area EBSD. A novel metric $E_p$ has been set up for a quantitative evaluation of the difference in pole figures. Visual

assessment has also been made by plotting the ODF difference in full Euler space. Finally, the influence of texture deviation between SXRD and EBSD on macro- and mesoscale simulation results is examined by the EPSC modelling approach. Thus providing insight into the reliability of two texture analysis methods from a visual and computational point of view.

Conclusions are summarised as below:

Texture refined from single shot Time-Of-Flight neutron diffraction pattern is based on cylindrical symmetry assumption and is presented in the form of inverse pole figure, which contains texture information in the direction of diffraction scattering vector of that pattern. No sample symmetry assumption is needed for single shot synchrotron X-ray diffraction pattern, and the result can be presented in the form of pole figures in complete projection space.

Inverse pole figures obtained from single shot Time-Of-Flight neutron diffraction reflect orientation distribution in an approximate manner, whilst detailed contour profile may be missing.

Pole figures constructed from single shot synchrotron X-ray diffraction pattern show decent match with those from EBSD in terms of max/min intensity and intensity distribution, with errors generally below 10%. The ODF difference is around ~0.1MRD for majority of full Euler space. Meanwhile, the inverse pole figures display more details than those from neutron diffraction. Inverse pole figures in Z direction are less accurate due to the lack of diffraction information.

On macroscale simulation result, the effect of texture deviation brought by the texture analysis technique is much less than that caused by the diversity of texture in different samples. On mesoscale, the texture deviation brings about no influence on the behaviour of grain groups in loading direction, whilst vertically, the lattice strain evolution paths show divergence in plastic regime but general tendencies remain consistent between EBSD and SXRD texture.

**Acknowledgements**

We are very grateful to Dr. Carlos N. Tomé from Los Alamos National Laboratory for authorising the access to EPSC simulation code (Version 4). AMK and ZW wish to acknowledge the support from EPSRC IAA Doctoral Impact Scheme grant EP/R511742/1. ZW is grateful for the support from Mr. Weizhong Wang and Mrs. Yong Qian. The authors would like to thank Diamond Light Source for allocation of beamtime MG25467 at I12 JEEP beamline.

**Data Availability**

The raw/processed data required to reproduce these findings cannot be shared at this time as the data also forms part of an ongoing study.

**References**

[1] Z. Wang, J. Chen, C. Besnard, A.M. Korsunsky, Microstructure evolution in a severely cold-worked NiTi wire during ageing treatment: An in situ neutron diffraction study, Materials Letters 281 (2020) 128676. https://doi.org/10.1016/j.matlet.2020.128676.

[2] U.F. Kocks, C.N. Tome, H.-R.Wenk, Texture and Anisotropy, Cambridge University Press 1998, United Kingdom.

[3] Z. Wang, A.M. Korsunsky, Effect of Temperature on Shape Memory Materials, Reference Module in Materials Science and Materials Engineering, Elsevier Inc. https://doi.org/10.1016/B978-0-12-803581-8.11793-X.

[4] Z. Wang, J. Chen, C. Besnard, L. Kuncicka, R. Kocich, A.M. Korsunsky, In-situ neutron diffraction investigation of texture-dependent Shape Memory Effect in a near equiatomic NiTi alloy, Acta Materialia 202 (2021) 135-148. https://doi.org/10.1016/j.actamat.2020.10.049.

[5] J. Chen, E. Salvati, F. Uzun, C. Papadaki, Z. Wang, J. Everaerts, A.M. Korsunsky, An experimental and numerical analysis of residual stresses in a TIG weldment of a single crystal nickel-base superalloy, Journal of Manufacturing Processes 53 (2020) 190-200. https://doi.org/10.1016/j.jmapro.2020.02.007.

[6] J. Chen, Z. Wang, A.M. Korsunsky, Multiscale stress and strain statistics in the deformation of polycrystalline alloys, International Journal of Plasticity (2022) 103260. https://doi.org/10.1016/j.ijplas.2022.103260.

[7] M. Knezevic, L. Capolungo, C.N. Tome, R.A. Lebensohn, D.J. Alexander, B. Mihaila, R.J. McCabe, Anisotropic stress-strain response and microstructure evolution of textured α-uranium, Acta Materialia 60 (2012) 702-715. https://doi.org/10.1016/j.actamat.2011.10.041.

[8] B. Clausen, C.N. Tome, D.W. Brown, S.R. Agnew, Reorientation and stress relaxation due to twinning: Modeling and experimental characterization for Mg, Acta Materialia 56 (2008) 2456-2468. https://doi.org/10.1016/j.actamat.2008.01.057.

[9] Z. Wang, J. Everaerts, E. Salvati, A.M. Korsunsky, Evolution of thermal and mechanical properties of Nitinol wire as a function of ageing treatment conditions, Journal of Alloys and Compounds 819 (2020) 153024. https://doi.org/10.1016/j.jallcom.2019.153024.

[10] E. Jimenez-Melero, N.H. van Dijk, L. Zhao, J. Sietsma, J.P. Wright, S. van der Zwaag, In situ synchrotron study on the interplay between martensite formation texture evolution and load partitioning in low-alloyed TRIP steels, Mater. Sci. Eng. A 528 (2011) 6407-6416. https://doi.org/10.1016/j.msea.2011.04.087.

[11] A. Pesach, E. Tiferet, S.C. Vogel, M. Chonin, A. Diskin, L. Zilberman, O. Rivin, O. Yeheskel, E.N. Caspi, Texture analysis of additively manufactured Ti-6Al-4V using neutron diffraction, Additive Manufacturing 23 (2018) 394-401. https://doi.org/10.1016/j.addma.2018.08.010.

[12] S. Kabra, S. Danion, W. Kockelmann, S.Y. Zhang, An neutron diffraction study of texture evolution under deformation in a hot rolled TWIP steel, Materials Today: Proceedings 2S (2015) S261-S266. https://doi.org/10.1016/j.matpr.2015.05.036.

[13] M.Y. Xie, N. Baimpas, C. Reinhard, A.M. Korsunsky, Texture analysis in cubic phase polycrystals by single exposure synchrotron X-ray diffraction, Journal of Applied Physics 114 (2013) 163502. https://doi.org/10.1063/1.4825120.

[14] L. Lutterotti, M. Voltolini, H.-R. Wenk, K. Bandyopadhyay, T. Vanorio, Texture analysis of a turbostratically disordered Ca-montmorillonite, American Mineralogist 95 (2010) 98-103. https://doi.org/10.2138/am.2010.3238.

[15] L. Lutterotti, R. Vasin, H.-R. Wenk, Rietveld texture analysis from synchrotron diffraction images. I. Calibration and basic analysis, Powder Diffraction 29 (2014) 76-84. https://doi.org/10.1017/S0885715613001346.

[16] L.R. Brandt, J.J. Marie, T. Moxham, D.P. Forstermann, E. Salvati, C. Besnard, C. Papadaki, Z. Wang, P.G. Bruce, A.M. Korsunsky, Synchrotron X-ray quantitative evaluation of transient deformation and damage phenomena in a single nickel-rich cathode particle, Energy Environmental Science 13 (2020) 3556-3566. https://doi.org/10.1039/D0EE02290J.

[17] F. Uzun, A.I. Salimon, E.S. Statnik, C. Besnard, J. Chen, T. Moxham, E. Salvati, Z. Wang, A.M. Korsunsky, Polar transformation of 2D X-ray diffraction patterns and the experimental validation fo the hDIC technique, Measurement 151 (2020) 107193. https://doi.org/10.1016/j.measurement.2019.107193.

[18] E.S. Statnik, A.I. Salimon, C. Besnard, J. Chen, Z. Wang, T. Moxham, I.P. Dolbnya, A.M. Korsunsky, Ovine Bone Morphology and Deformation Analysis Using Synchrotron X-ray Imaging and Scattering, Quantum Beam Science 4(3) (2020) 29. https://doi.org/10.3390/qubs4030029.

[19] F. Hofmann, B. Abbey, L. Connor, N. Baimpas, X. Song, S. Keegan, A.M. Korsunsky, Imaging of grain-level orientation and strain in thicker metallic polycrystals by high energy transmission micro-beam Laue (HETL) diffraction techniques, International Journal of Materials Research 103 (2012) 192-199. https://doi.org/10.3139/146.110660.

[20] B.H. Toby, R.B. Von Dreele, GSAS-II: the genesis of a modern open-source all purpose crystallography software package, Journal of Applied Crystallography 46 (2013) 544-549. https://doi.org/10.1107/S0021889813003531.

[21] S. Takajo, S.C. Vogel, Determination of pole figure coverage for texture measurements with neutron time-of-flight diffractometers, Journal of Applied Crystallography 51 (2018) 895-900. https://doi.org/10.1107/S1600576718007732.

[22] L. Lutterotti, M. Bortolotti, G. Ischia, I. Lonardelli, H.-R. Wenk, Rietveld texture analysis from

diffraction images, Z. Kristallogr. Suppl. 26 (2007) 125-130.
[23] F. Uzun, C. Papadaki, Z. Wang, A.M. Korsunsky, Neutron strain scanning for experimental validation of the artificial intelligence based eigenstrain contour method, Mechanics of Materials 143 (2020) 103316. https://doi.org/10.1016/j.mechmat.2020.103316.
[24] C. Papadaki, W. Li, A.M. Korsunsky, On the Dependence of $\gamma'$ Precipitate Size in a Nickel-Based Superalloy on the cooling Rate from Super-Solvus Temperature Heat Treatment, Materials 11 (2018) 11 1528. https://doi.org/10.3390/ma11091528.
[25] F. Bachmann, R. Hielscher, H. Schaeben, Texture analysis with MTEX-Free and open source software toolbox, Solid State Phenom. 160 (2010) 63-68. https://doi.org/10.4028/www.scientific.net/SSP.160.63.
[26] P. Staron, A. Schreyer, H. Clemens, S. Mayer, Neutrons and Synchrotron Radiation in Engineering Materials Science, Wiley-VCH (2017) 73-123.
[27] R.B. Von Dreele, Quantitative texture analysis by Rietveld refinement, Journal of Applied Crystallography, 30 (1997) 517-525. https://doi.org/10.1107/S0021889897005918.
[28] H.J. Bunge, Texture analysis in Materials Science: Mathematical Methods, London: Butterworth-Heinemann (1982) 49-57.
[29] R. Hielscher, H. Schaeben, A novel pole figure inversion method: specification of the MTEX algorithm, Journal of Applied Crystallography 41 (2008) 1024-1037. https://doi.org/10.1107/S0021889808030112.
[30] H.J. Bunge, Texture Analysis in Materials Science, Mathematical Methods. London: Butterworths (1982).
[31] H. Wang, B. Clausen, C.N. Tome, P.D. Wu, Studying the effect of stress relaxation and creep on lattice strain evolution of stainless steel under tension, Acta Materialia 61 (2013) 1179-1188. https://doi.org/10.1016/j.actamat.2012.10.027.
[32] C.J. Neil, J.A. Wollmershauser, B. Clausen, C.N. Tome, S.R. Agnew, Modelling lattice strain evolution at finite strains and experimental verification for copper and stainless steel using in situ neutron diffraction, International Journal of Plasticity 26 (2010) 1772-1791. https://doi.org/10.1016/j.ijplas.2010.03.005.